THE COMPANY OF
Biologists

RESEARCH ARTICLE

The hydrodynamics of swimming at intermediate Reynolds numbers in the water boatman (*Corixidae*)

Victoria Ngo and Matthew James McHenry*

ABSTRACT

The fluid forces that govern propulsion determine the speed and energetic cost of swimming. These hydrodynamics are scale dependent and it is unclear what forces matter to the tremendous diversity of aquatic animals that are between a millimeter and a centimeter in length. Animals at this scale generally operate within the regime of intermediate Reynolds numbers, where both viscous and inertial fluid forces have the potential to play a role in propulsion. The present study aimed to resolve which forces create thrust and drag in the paddling of the water boatman (Corixidae), an animal that spans much of the intermediate regime ($10<Re<200$). By measuring the force generated by tethered water boatmen, we found that thrust is generated primarily by drag on the paddling appendages, with a negligible contribution from the acceleration reaction force. Based on these findings, we developed a forward-dynamic model of propulsion in free swimming that accurately predicted changes in the body's center of mass over time. For both tethered and free swimming, we used non-linear optimization algorithms to determine the force coefficients that best matched our measurements. With this approach, the drag coefficients on the body and paddle were found to be up to three times greater than on static structures in fully developed flow at the same Reynolds numbers. This is likely a partial consequence of unsteady interactions between the paddles or between the paddles and the body. In addition, the maximum values for these coefficients were inversely related to the Reynolds number, which suggests that viscous forces additionally play an important role in the hydrodynamics of small water boatmen. This understanding for the major forces that operate at intermediate Reynolds numbers offers a basis for interpreting the mechanics, energetics and functional morphology of swimming in many small aquatic animals.

KEY WORDS: Modeling, Acceleration reaction, Thrust, Drag, Propulsion

INTRODUCTION

The speed of swimming and its energetic requirements are determined by hydrodynamics that vary with the speed and size of an animal. The Reynolds number is a fundamental metric of hydrodynamic scaling that approximates the ratio of inertial to viscous forces. At intermediate Reynolds numbers ($1<Re<1000$), all viscous and inertial forces have the potential to contribute to thrust and drag. It is in this domain that a tremendous diversity of aquatic animals operate while swimming. The aim of the present study was to resolve which forces play a role in the paddling of the water

Department of Ecology and Evolutionary Biology, University of California, Irvine, CA 92697 USA.

*Author for correspondence (mmchenry@uci.edu)

boatman (Corixidae), an animal that operates in the intermediate regime ($10<Re<200$) (Blake, 1986).

A swimming animal must generate thrust to overcome drag. Drag acts in the direction of flow velocity, which is in opposition to the velocity of a body moving through a still pool of water. A paddling swimmer creates thrust by rapidly moving its appendages posteriorly during a power stroke (Fig. 1). This is considered 'drag-based' thrust because it is drag on the appendages that creates thrust for the body (Alexander, 1968). At the scale of the paddles or the body, drag may be created by a combination of skin friction and pressure drag. Skin friction emerges from the viscous resistance of water to shearing and it varies in direct proportion to flow velocity. It is the dominant force in the low Reynolds number ($Re<1$) propulsion of microorganisms. Pressure drag is created by stream-wise differences in velocity over a body's surface. Its magnitude varies in proportion the square of flow velocity (Lamb, 1945) and is dominant at high Reynolds numbers ($Re>1000$). For unsteady motion, such as that generated by an oscillating appendage, additional force may be generated by the added mass of water carried by a structure as it accelerates and decelerates. This acceleration reaction force varies in proportion to the volume of water entrained by the structure (Lamb, 1945). Therefore, skin friction, pressure drag and acceleration reaction could all play a role in swimming at intermediate Reynolds numbers.

The present study examined the relative magnitude of each of these forces in the swimming of water boatmen. Paddling by this aquatic insect is achieved by the motion of the metathoracic hindlegs. The tarsus (i.e. the most-distal) segment of this limb functions as a paddle (Blake, 1986). This paddle includes an array of setae that splay during the power stroke and collapse during the recovery stroke. This motion is similar to swimming in water beetles (Dytiscidae), which was classically investigated by Nachtigall (Nachtigall and Bilo, 1965). Both have provided a seemingly simple subject for hydrodynamic investigation (Daniel, 1984; Blake, 1986) and a textbook case for introducing biological propulsion (Alexander, 2003). Through mathematical modeling and kinematic measurements, these studies suggest that the acceleration reaction and pressure drag are important contributors to propulsion. We first tested this idea by measuring the thrust generated by tethered water boatmen (Figs 1, 2). These measurements were compared against the predictions of models that differed in their inclusion of the three fluid forces under consideration. We found the force coefficients for each model that best fitted the force measurements using a non-linear optimization routine (Fig. 3). The results of the tethered swimming experiments then provided the basis of a forward dynamic model of the hydrodynamics of free swimming. By additionally simulating drag on the body, this model predicted the center-of-mass changes in speed through time. Upon verifying these predictions against measurements of body kinematics, we were able to infer the major forces during swimming and their energetic implications.

List of symbols and abbreviations

C_B	drag coefficient of the body
C_P	inertial drag coefficient of the appendage
C_V	viscous drag coefficient of the appendage
E_D	energy lost to drag
E_K	total kinetic energy
E_P	energy generated by the paddle
E_T	energy from thrust
EI	flexural stiffness
F	magnitude of a point-load on a beam
l	characteristic length
l_d	depth of the body
l_L	distance from the base of the tether to the point of load application
l_P	length of the paddle
l_T	distance from the base of the tether to the midpoint of body depth
l_w	width of the body
m	mass of the insect
P_D	power lost to drag
P_P	instantaneous power generated by the paddle
P_T	power generated by thrust
Re	Reynolds number
Re_P	Reynolds number on the appendage
Re_B	Reynolds number on the body
s_B	projected area of the body
s_P	paddle area
T_A	thrust created by acceleration reaction
T_D	thrust created by pressure drag
T_M	measured thrust
T_V	thrust created by viscous drag
u	characteristic speed
u_B	speed of the body
u'_B	acceleration of the body
u_P	speed of the paddle
u'_P	acceleration of the paddle
v_P	volume of water around the paddle
x	body position
α_B	force coefficient of acceleration reaction on the body
α_P	added mass coefficient of the paddle
γ	cost of transport
δ	deflection
η_K	propulsive efficiency
η_T	efficiency of generating thrust
θ	paddle angle
μ	dynamic viscosity of water, 1.002 Pa s
ρ	density of water, 1000 kg m^{-3}
ϕ	wrist angle

RESULTS

The hydrodynamics of tethered swimming

We successfully tested mathematical models of thrust with measurements in tethered water boatmen. High-speed video recordings of the power stroke (e.g. Fig. 4A) showed how the extended hindlimbs moved smoothly from the anterior-most position toward the posterior (45 deg<ϕ<165 deg, where ϕ is wrist angle). The hindlegs reversed direction during the recovery stroke, as the paddles flexed to align with the long axis of the body (Fig. 4B). The angle (Fig. 4C) and velocity (u_P, Fig. 4D) of the paddle, in combination with morphometrics (Fig. 2F, Table 1), provided the necessary inputs to model thrust. Models for both pressure drag and skin friction predicted peak thrust with a timing that was coincident with measured thrust (Fig. 4E), which occurred approximately when the speed of the power stroke was greatest (Fig. 4D). However, only the pressure drag model was found to increase rapidly enough to match the magnitude of our measured changes in force (red curve in Fig. 4E). The rapid change in thrust by pressure drag was due to
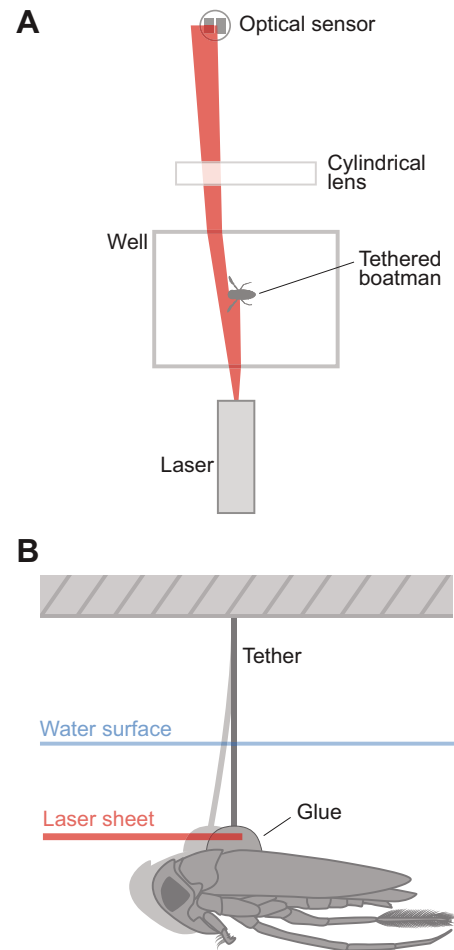

Fig. 1. Experimental setup for thrust measurements. (A) A dorsal view of the setup illustrating the positioning of the sheet-generating laser, cylindrical lens and optical sensor that allow for fine-scale measurements of the deflection of a tethered water boatman. (B) A lateral view of the boatman shows where the laser sheet was obscured by a mound of glue on the submerged dorsal surface of the boatman. The shadow cast by the glue increased as the tether deflected (in light gray, exaggerated for illustration) during a power stroke. These changes in the position of the shadow were detected by the optical sensor.

the dependency of this force on the square of paddle velocity. Skin friction, which varies in direct proportion to velocity, failed to predict these rapid changes in thrust (blue curve in Fig. 4E).

Because of the superior matching of the pressure drag model, we calculated the difference between its prediction and our measurements to consider any additional force that could play a role in thrust generation. The signal of this residual thrust (Fig. 4F) was not substantially greater than the high-frequency electrical noise of our measurements. Some sequences exhibited occasions where force measurements appeared to coincide with predictions for thrust from acceleration reaction (e.g. the first green curve in Fig. 4F). These occasions offer an indication that the acceleration reaction could be a minor contributor to thrust at the beginning of a power stroke (Fig. 4D).

We tested the accuracy of each model by comparing predictions for the momentum generated during the power stroke against measurements (Fig. 5). Accuracy was evaluated by calculating the coefficient of determination for model predictions against the measurements. Over the range of our momentum measurements (from 0.4 to 9.5 g mm s^{-1}), the skin friction model (Eqn 4) predicted
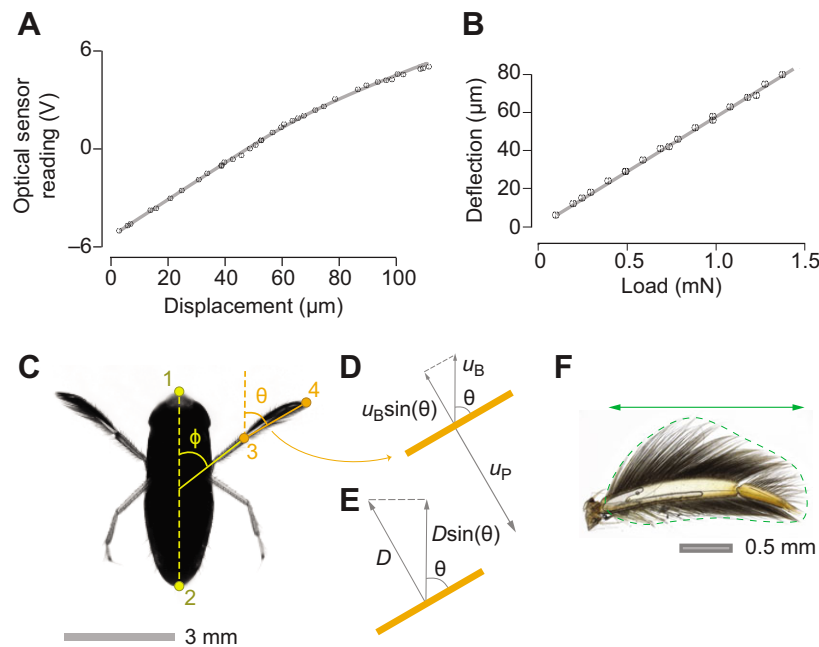
Fig. 2. Methods employed in tethering experiments. (A,B) A two-part calibration was conducted after each tethering experiment to calculate thrust from deflection measurements (Fig. 1). (A) By varying the position of the tether with a micrometer, we established a relationship between deflection and the voltage reading of our optical sensor. This relationship was characterized by a smoothing spline (gray curve). (B) By hanging weights near the end of the tether, we determined the relationship between this load and the deflection that it created. This relationship was characterized by a linear least-squares curve fit (gray curve). As detailed in Materials and methods, these two relationships provided the basis for calculating thrust for our tethering experiments. (C) High-speed video recordings of the water boatmen from a ventral view permitted measurement of the kinematics of the hindlegs. This image was extracted from a single frame of video to illustrate the position of landmarks that were manually tracked in our analysis. This included coordinates for (1) the anterior margin of the body, (2) the posterior margin of the body, (3) the joint between the tarsus and tibia and (4) the distal margin of the tarsus (i.e. paddle). (D) Schematic diagram of the paddle (orange line) illustrating the geometry of the body (u_B) and paddle (u_P) velocities that factor into the calculation of drag (D) generated by the paddle (Eqns 3, 4 and 8). (E) The thrust generated by the paddle is equal to the forward component of the drag on the paddle [$T=D\sin(\theta)$]. (F) A single paddle with its setae splayed under the compression of a microscope slide. The area encompassed by the setae (dashed green curve) and its greatest linear dimension (solid green line) were measured for each water boatman.

only about one-quarter of the variation in measured momentum ($R^2=0.25$, $N=9$). This was the result of an inability of the skin friction model to match the rapid changes in thrust that we observed (Fig. 4E). In contrast, the pressure drag model (Eqn 5) predicted almost all variation in measured momentum ($R^2=0.98$, $N=9$). Note that this result does not preclude a role for skin friction as a contributor to propulsion, which is an issue we addressed by examining variation in the drag coefficient with Reynolds number (discussed below). Adding acceleration reaction (Eqn 5) to the pressure drag model increased the predicted momentum a small amount (~0.2 g mm s^{-1}), but this did not enhance the accuracy of the predictions ($R^2=0.97$, $N=9$). Therefore, pressure drag on the paddle alone was sufficient to predict the momentum generated by a tethered water boatman.

The hydrodynamics of free swimming

We applied our findings on the hydrodynamics of tethered swimming to a model of a freely swimming water boatman. When untethered, the paddling of the hindlimbs served to propel the water boatmen forward (Fig. 6A,B). During the power stroke, the posterior-directed motion of the paddle was reflected in an increase in the wrist and paddle angles (Fig. 6C) and a rapid negative velocity (Fig. 6D). Simulations of our forward-dynamic model predicted oscillations in swimming speed in a manner similar to our kinematic measurements (Fig. 6E). Based on the results of our tethering experiments (Fig. 5), this model (Eqn 8) assumed that thrust was generated solely by drag on the paddle. Therefore, its predicted

thrust (Fig. 6F) roughly coincided with the large changes in paddle velocity during a power stroke (Fig. 6D). As thrust was imparted momentum to the body, the body increased in speed and thereby encountered greater drag. This drag caused the body to decelerate as the velocity of the paddle declined at the end of the power stroke and increased through the recovery stroke.

The energetics of swimming were considered by analyzing the results of each simulation. When a water boatman was accelerating (e.g. the first power stroke in Fig. 6G), the total power generated by the paddle necessarily exceeded the thrust power. As the body moved forward at higher speed, the flow created by body motion enhanced thrust power (the final term in Eqn 13), but adversely affected the power generated by the paddle (Eqn 12). As a consequence, thrust power could exceed that generated by the paddle as the body gained speed (e.g. the second and third power strokes in Fig. 6G). However, the total energy generated by thrust could not exceed that generated by the paddle (Fig. 6H) for a water boatman starting from rest. The kinetic energy, and hence the speed, increased when thrust exceeded drag during the power stroke. During the recovery stroke, drag succeeded in dissipating the energy of propulsion (Fig. 6H) and thereby reducing the speed of the body (Fig. 6E).

The accuracy of our forward dynamic model was tested by comparing its predictions of body speed against our measurements. Similar to our tethered measurements of momentum (Fig. 5), we tested the model predictions of swimming speed against measurements by calculating a coefficient of determination with
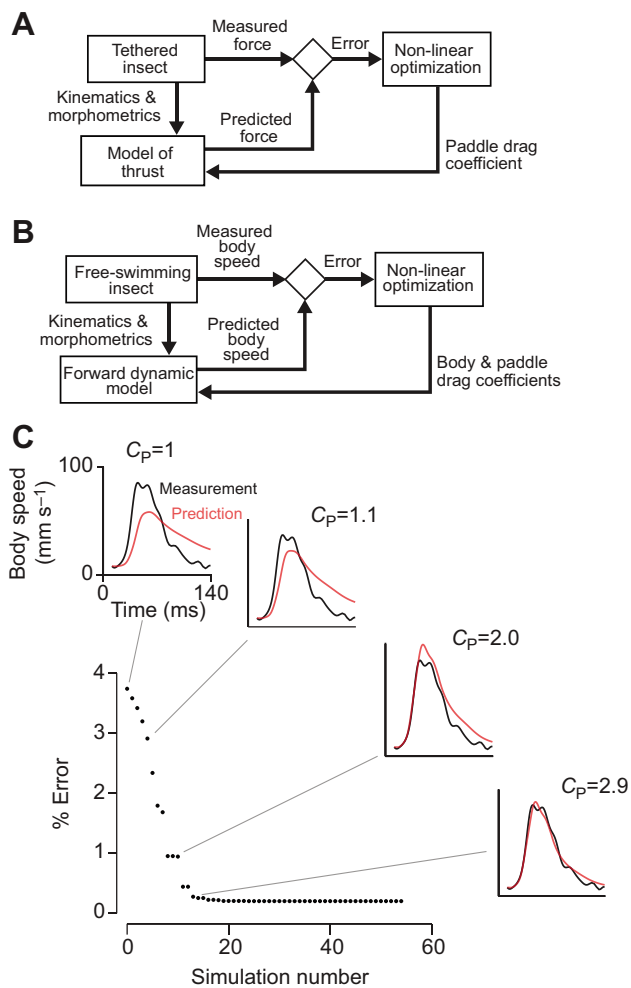
Fig. 3. Non-linear optimization for determining force coefficients. Using a least-squares approach, these optimizations were performed to find the drag coefficients for (A) tethered and (B,C) free swimming that generated predictions that best fitted our measurements. (A) A hydrodynamic model formulated a prediction for thrust that was based on our measurements of the kinematics and morphometrics of the paddle (Eqns 4–6). The optimization attempted to minimize the error between this prediction and our measurement by varying the drag coefficient for the paddle over a series of simulations. (B) The optimization for free swimming operated in a similar manner, but the error between predicted and measured body speed was the quantity that the optimization sought to minimize. (C) A representative optimization demonstrates how the percent error between measured (black curve in the insets) and predicted (red curve) body speed decreased monotonically over a series of simulations (the four insets display sample simulations) run by the optimization algorithm for a power stroke during free swimming.

respect to unity. Variation in the mean speed of the body over the duration of a swimming cycle was well predicted by the model (R^2=0.90, N=13; Fig. 7A). Variation in the maximum speed was similarly predicted by the model (R^2=0.85, N=13; Fig. 7B). Therefore, our forward dynamic model (Eqn 8) accurately predicted the swimming speed of water boatmen.

Drag, energetics and Reynolds number
Our kinematic measurements verified that water boatmen operate at intermediate Reynolds numbers. The Reynolds number values for both the paddle (Re_P, Fig. 8A) and whole body (Re_B, Fig. 8B) were positively correlated with body length. For free-swimming

experiments, we used water boatmen that spanned a nearly threefold range in body length (2.7 mm≤l_B≤7.7 mm, N=12), where the Reynolds numbers of the paddle (3≤Re_P≤70) were lower than those for the body (24≤Re_B≤280). The tethered water boatmen spanned a more narrow range of body lengths (5.0 mm≤l_B≤8.8 mm, N=9) and Reynolds numbers (31≤Re_P≤130) that overlapped with the values of free-swimming animals. Therefore, the paddling of tethered and free-swimming animals operated in a similar hydrodynamic regime.

The relationship between drag coefficient and Reynolds number can offer valuable insight into the mechanisms of force generation. These coefficients were found by using optimization algorithms that minimized error between the model and measurements (Fig. 3). The greatest values for the drag coefficient for both the body and paddle were achieved at the lowest Reynolds numbers, which were generated by the smallest individuals (Fig. 8A). Furthermore, the range of the drag coefficient was substantially greater at lower Reynolds numbers. For example, the drag coefficient for the paddle (C_P) varied by about an order of magnitude for Re<30 (1.2<C_P<11.6, N=7), but showed not even a threefold range of variation at Re>75 (0.6<C_P<1.6, N=2; Fig. 9A). A similar trend was observed for the body of a water boatman, though with a more narrow range of variation in the drag coefficient (1.2<C_B<5.6, N=7), over a wider range of variation in Reynolds number (Fig. 9B).

Our modeling allowed for a consideration of the energetics of propulsion. We found that the energetic cost of generating thrust (8.7±7.3 J kg^{-1} m^{-1}, N=13) accounted for about two-thirds of the total cost of transport (γ=13.0±10.4 J kg^{-1} m^{-1}, N=13). The remaining one-third of this cost was lost to the generation of lateral forces. Although the mass of the body and surrounding water resists acceleration during the power stroke, this mass also acts to maintain an elevated speed during the recovery stroke. Therefore, mass has a neutral effect on the cost of transport. Because of the generation of lateral forces, the thrust efficiency (Eqn 17) was 72% (η_T=0.72±0.49, N=13), whereas the propulsive efficiency, which reflects the overall efficiency of generating kinetic energy (Eqn 17), was merely 10% (η_K=0.10±0.09, N=13). Therefore, inefficiency generated by drag far exceeds the losses due to lateral forces.

DISCUSSION
Our findings establish the major forces that govern the swimming hydrodynamics of the water boatman. Through experiments on tethered and free-swimming animals, we found that thrust is principally created by pressure drag on the paddle. However, viscous forces play a role by both contributing to propulsion and enhancing drag on the body. This role for viscosity is particularly important for the smaller water boatmen that operate at lower Reynolds numbers. At this scale, drag generated on the paddle and body greatly exceeds the quasi-steady values expected for each in isolation. Therefore, unsteady viscous interactions between the paddles and the body affect propulsion at the lower end of the intermediate Reynolds number regime. These principles may be applied toward understanding swimming in a broad diversity of animals.

The acceleration reaction
The acceleration reaction has the potential to contribute to thrust at the start of a power stroke, as the mass of water entrained by the paddle is maximally accelerated toward the posterior of the body (Daniel, 1984). Previous studies on dytiscid beetles (Nachtigall, 1960) and water boatmen (Blake, 1986) appear to support this as a source of propulsion. Blake estimated the momentum from the acceleration reaction to be roughly equivalent to that generated by drag (Blake, 1986). His model employed the conventional
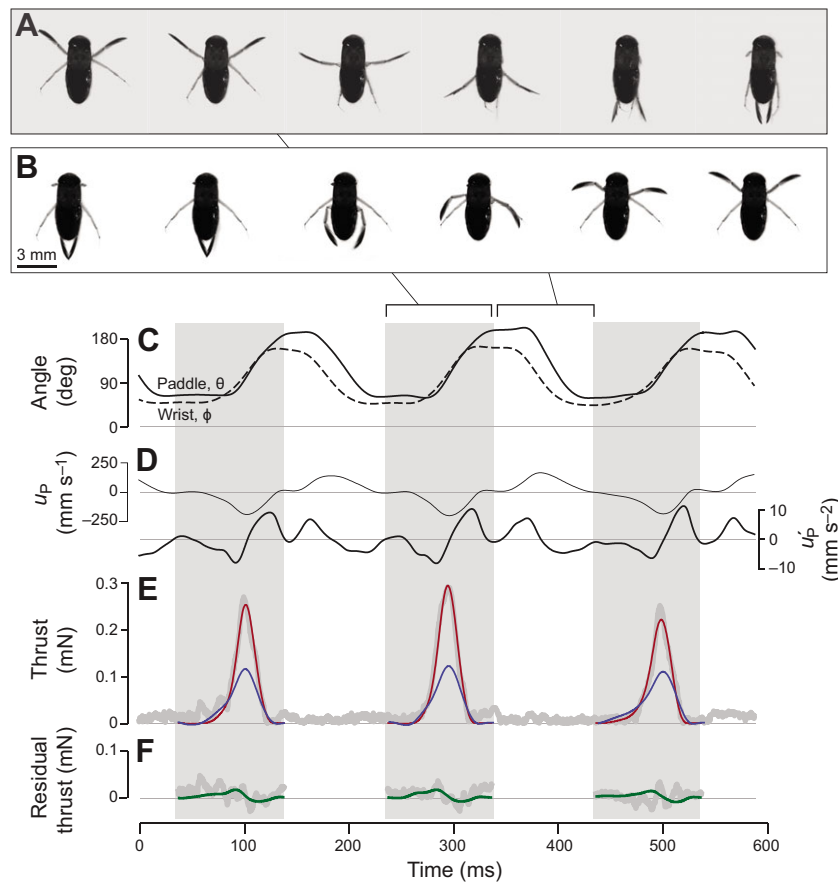
Fig. 4. A representative thrust measurement for tethered water boatmen. Video frames of (A) the power stroke and (B) the recovery stroke illustrate the motion of the hindlegs that create thrust (15 ms intervals). (C,D) Kinematic parameters provided input variables to mathematical models of thrust. (C) Measurements of the paddle angle (θ, solid curve) determine the direction of force generated by the paddle. The wrist angle (ϕ, dashed curve) was used to define the duration of the power strokes (gray bars). (D) The paddle speed (u_P, thin curve) affects the pressure drag (Eqn 3) and skin friction (Eqn 4) generated by the paddle and its acceleration ($\dot{u}_P$, thick curve) affects the acceleration reaction (Eqn 5). (E) The thrust predicted by these models was compared with measurements of thrust (thick gray curve). The force coefficients for thrust from pressure drag (red curve) and skin friction (blue curve) were determined by non-linear optimization (Fig. 3A) to provide the best match to the measurement for each model of thrust. (E) The residual thrust was calculated as the difference between measured thrust (gray curve in E) and thrust from pressure drag (red curve in E). The prediction for thrust by acceleration reaction (green curve) was fitted to this residual force for the power stroke.

assumption that the paddle accelerates a volume of water equal to a cylinder with the same dimensions. However, measurements of thrust in a dynamically scaled model of *Artemia* paddles found no evidence for an early thrust peak that would be expected from this added mass (Williams, 1994). These model measurements were performed at relatively low Reynolds numbers (*Re* ~5) compared with those of water boatmen (Fig. 9), but they suggested that force generated by the added mass may be smaller than previously

considered. Our results agree with Williams' findings, as we found no consistent peak in thrust early in the power stroke (Fig. 4E). Furthermore, the inclusion of the acceleration reaction in our model did not enhance the accuracy of momentum predictions for tethered swimming (Fig. 5).

The acceleration reaction has similarly been shown to play only a minor role in other modes of locomotion at intermediate Reynolds numbers. This force is not an important source of propulsion in

Table 1. Morphometrics and model parameters

	m (g)	L (mm)	L_W (mm)	L_D (mm)	s_P (mm^2)	l_P^2	l_T^2	l_L^2	α_B
Tethered	4.8	4.98	1.75	1.74	0.12548	1.85	10.33	8.17	
	5.6	5.37	1.88	1.33	0.17497	1.99	8.35	5.54	
	6.6	5.44	2.11	1.87	0.19743	2.07	10.12	8.62	
	7.2	5.68	2.19	1.90	0.19656	2.13	10.12	8.38	
	7.3	5.35	2.05	2.01	0.21290	2.03	9.59	8.39	
	7.4	5.58	2.29	1.90	0.16640	2.14	8.56	7.02	
	7.9	8.78	2.22	1.93	0.22535	3.21	7.95	5.31	
	9.0	7.70	2.33	1.97	0.25347	2.85	8.65	6.41	
	10.6	6.63	2.21	1.95	0.18847	2.43	10.68	7.29	
Free swimming	0.2	2.75	1.32	0.60	0.02682	1.78			0.15
	0.3	2.70	1.31	0.61	0.01215	1.55			0.14
	1.0	2.67	1.32	0.74	0.25879	1.14			0.15
	3.5	4.68	1.48	1.33	0.09550	1.82			0.10
	3.6	4.71	1.59	1.25	0.08956	1.89			0.10
	3.6	4.65	1.41	1.30	0.08047	1.39			0.99
	3.8	4.10	1.70	1.34	0.01062	1.35			0.16
	7.0	6.00	2.53	1.87	0.22191	0.72			0.14
	14.7	7.51	2.61	2.40	0.25895	1.31			0.12

All values are a single measurement except for the added mass coefficient, α_B, which was calculated from Eqn 8.
m, body mass; L, body length; L_W, body width; L_D, body depth; s_P, area of the paddle; l_P, length of the paddle; l_T, distance from the base of the tether to the midpoint of body depth; l_L, distance from the base of the tether to the point of load application.
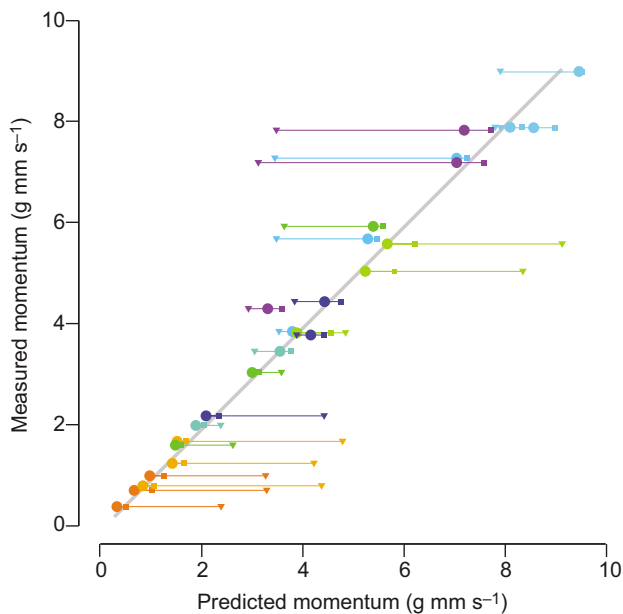
Fig. 5. The accuracy of models of thrust in tethered water boatmen. Power strokes were predicted by three models, each presented here with a unique symbol. For each power stroke in an experiment, the momentum predicted by each model is plotted against the momentum measured for the same power stroke. The three model predictions are linked by a horizontal line and each individual is uniquely color coded. Deviation from the unity line (gray curve) represents inaccuracy in the prediction of a model. Thrust generated solely by pressure drag on the paddle (filled circles) showed little deviation from the unity line (R^2=0.98, N=9). This model was not improved by adding the momentum generated by the acceleration reaction (filled squares, R^2=0.97). The thrust generated by skin friction on the paddle (filled triangles) yielded highly inaccurate predictions of momentum (R^2=0.25).

tethered and free-swimming ascidian larvae, which swim by tail undulation at Re ~100 (McHenry et al., 2003). It is perhaps not surprising, given the low density of air, that the acceleration reaction is also negligible in the lift generation of flies, which operate in a similar regime (Re ~140) (Dickinson et al., 1999). The acceleration reaction does appear to generate thrust in the impulsive accelerations of the chaetognath (*Sagitta elegans*), which attain relatively high intermediate Reynolds numbers (Re ~1000) (Jordan, 1992). At the larger scales of adult fish, the acceleration reaction also contributes to propulsion for steady swimming (Lighthill, 1971; Tytell, 2004; Wu, 1971) and accelerations (Frith and Blake, 1991; Tytell and Lauder, 2008; Weihs, 1972). Therefore, the acceleration reaction can act as an important source of propulsion for swimming in relatively large animals and perhaps in rapid accelerations at the high end of the intermediate Reynolds number regime.

Thrust and drag

Our findings allow for a nuanced interpretation of the role of viscosity in propulsion at this scale. We found that skin friction was insufficient to explain the rapid rise in thrust that was generated during the power stroke (Fig. 4E). As a consequence, this force alone failed to predict the momentum generated by tethered swimming (Fig. 5). However, this result does not preclude a role for viscosity in the generation of thrust. The drag coefficient represents force that is normalized by parameters that determine pressure drag. Therefore, the drag coefficient is predicted to be invariant with respect to Reynolds number where drag is generated entirely from the pressure differences that emerge from laminar flow. These

conditions are violated at lower Reynolds numbers, where viscosity significantly contributes to drag. This occurs on a sphere, where skin friction causes the drag coefficient to elevate with decreasing Reynolds number (Fig. 9B). Williams found a similar trend for drag on the appendages of *Artemia*, which include an array of setae that are similar to the hindlegs of a water boatman (Williams, 1994). It is therefore unsurprising that we found a similar pattern for both free-swimming and tethered water boatmen for the drag on the paddle (Fig. 9A) and on the body (Fig. 9B). We consequently conclude that viscosity contributes to the generation of both thrust and drag, especially in small water boatmen. However, even when accounting for the effect of skin friction, small water boatmen generated larger forces than expected.

The range and maximum values for the drag coefficient that we measured for the body of a water boatman exceed the precedents in the literature. Jumping terrestrial insects span the intermediate regime and exhibit drag coefficient values that approximate unity. Blake found similar values by fitting a model of drag to the free swimming of a single water boatman (Blake, 1986). Lower values (C_B ~0.4) have been reported for water beetles (Dytiscidae), which paddle like water boatmen but at higher Reynolds numbers (up to Re ~10^5) (Nachtigall, 1960). These values for drag coefficient approximate those of ellipsoidal bodies at comparable Reynolds numbers (Hoerner, 1965). In contrast, we found drag coefficients for the body that were up to an order of magnitude greater than in water beetles and at least fivefold greater than other insects (Fig. 9B). These values originated by fitting our forward-dynamic model to measurements of body speed (Fig. 3B). Therefore, lower drag coefficient values would have caused the model to fail to replicate the rapid decline in speed that we observed during the recovery stroke (Fig. 6E) and thereby not achieve the same accuracy in our predictions (Fig. 7).

We recognize a few possible explanations for the discrepancy between our values for drag coefficient and prior studies. First, the Reynolds numbers are lower in water boatmen than in jumping insects and water beetles. For reasons described above, skin friction should elevate the drag coefficient at low Re (Fig. 9B). In addition, the body of a water boatman is likely exposed to flow above what is explicitly considered by our model (Jiang and Kiørboe, 2011). The paddles induce flow past the body that should act to augment drag during the power stroke. Vortex shedding by the paddles should create flow, and consequently low pressure, at the posterior of the body. This would function to enhance drag at the transition between power and recovery strokes. Finally, although we observed no force generation during the recovery stroke in our tethering experiments (Fig. 4E), it remains possible that the recovery stroke motion of the paddles could contribute to drag in free swimming (Blake, 1986).

Our measurements for the drag coefficient of the paddle are also greater than values reported in prior studies. The drag for an *Artemia* appendage was found to approximate that of a cylinder of comparable dimensions (Williams, 1994). As in our measurements, these values increased at lower Reynolds numbers, presumably due to skin friction. However, we found the drag coefficient to be twofold or threefold greater than that of a cylinder in this regime (Fig. 9A) for reasons that are unclear. These large values are not due to the porosity of the paddle, because a semi-porous appendage does not exceed the force-generating capacity of a solid cylinder (Cheer and Koehl, 1987a; Cheer and Koehl, 1987b). It is possible that a combination of unsteady mechanisms and fluid–structure interactions account for the high thrust generated by water boatmen. For example, the paddles should create a 'starting vortex' at the initiation of a power stroke that establishes the circulation for thrust
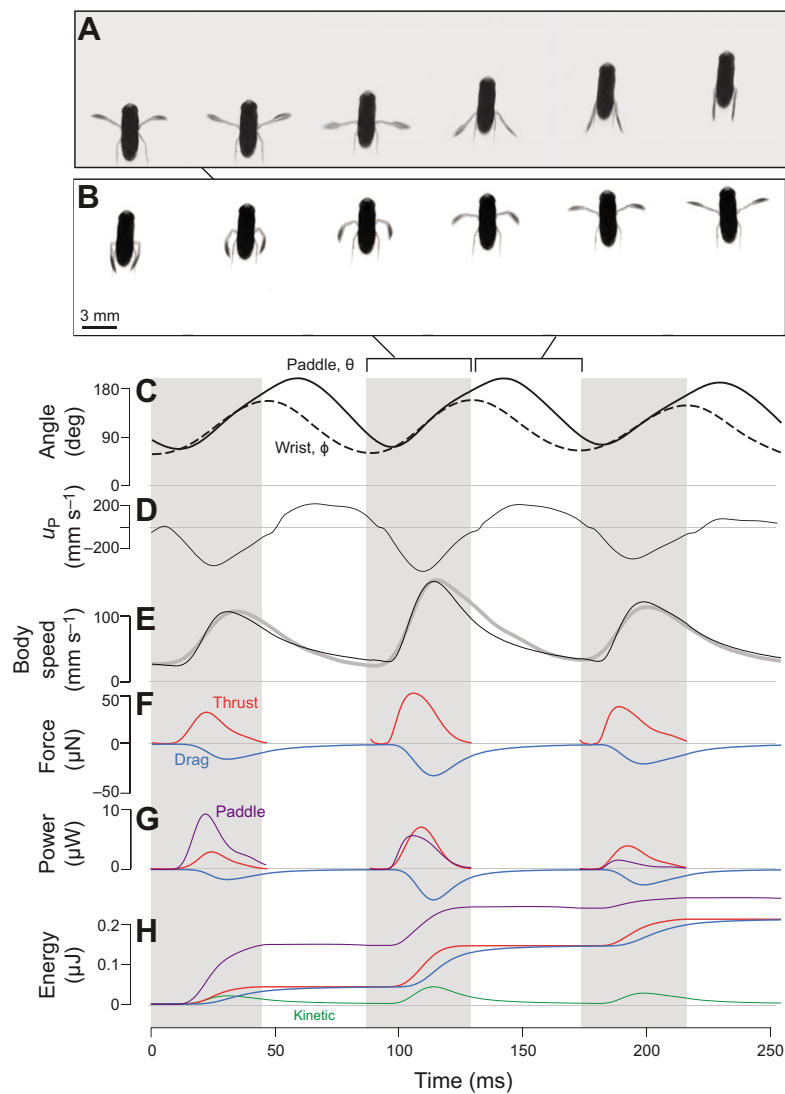
Fig. 6. Kinematics and hydrodynamics of free swimming.
High-speed video recordings of (A) the power and (B) the recovery strokes for a water boatman (8 ms intervals) revealed a similar paddling motion to tethered swimming (Fig. 4), but here the insect was free to advance forward. (C) Reversals in the wrist angle were used to define the duration of the power strokes (gray bars). We measured (C) the angle and (D) the velocity (u_P) of the paddle (relative to the body) to model thrust. Forward dynamic simulations included thrust and drag on the body to predict changes in the speed of the body over time (Eqn 8). (E) These predictions of speed (black curve) were tested against measurements (gray curve) for the same sequence. (F) The thrust (red curve) predicted by this model peaked at around the middle of the body stroke as the total drag generated by the body and appendages (blue curve) lagged behind in time, as the body gained speed as a result of the thrust impulse. (G) The power generated by the paddle (purple curve, Eqn 11) and that applied to thrust (red curve, Eqn 12) are plotted with the power lost through the generation of drag (blue curve, Eqn 13). The peak thrust power progressively exceeded the power generated by the paddle as a result of the increased body velocity across power strokes. (H) These values for power were integrated over time in comparison to the kinetic energy of the body (green curve, Eqn 15).

(Dickinson, 1996). Each paddle may interact with the paddle on the contralateral side to create a vortex loop that enhances the circulation, and therefore thrust, of both paddles. Such a mechanism could break down at higher *Re*, as a result of less viscous cohesion in the flow field. Although unsteady mechanisms of this sort have been shown to be ineffective at lower *Re* values in insect flight (Miller and Peskin, 2009), the geometry and motion of water boatmen may offer a contrast. Future flow visualization and mathematical modeling studies could resolve how a water boatman creates the very large force coefficients that we report here.

The energetics of swimming

Hydrodynamics greatly determine the energetic cost of swimming. Owing to the relatively large drag coefficients that we measured, the cost of transport that we determined for water boatmen is relatively high. By comparison, a 5 g larval fish that swims at its most efficient speed requires a metabolic cost of transport of ~9.4 J kg^{-1} m^{-1} (Kaufmann, 1990; Videler, 1993). If one assumes the maximal efficiency of 50% for the red muscle of fish (Curtin and Woledge, 1993), then a mechanical cost of transport of 4.7 J kg^{-1} m^{-1} is predicted. This conservative estimate is comparable to the most energetically economical water boatmen that we have modeled (Fig. 10A). However, because of the many instances of higher values, we found a mean cost of transport that was about threefold

greater than this approximated value for larval fish (γ=13.0±10.4 J kg^{-1} m^{-1}, *N*=13). Although fast swimming may elevate the cost of transport by a factor of 2 or 3 in fish larvae (Kaufmann, 1990), we found some water boatmen exceeded this estimate by an order of magnitude (Fig. 10A). This may be due to the high inefficiency of paddling. Larval fish swim with a propulsive efficiency of around 0.3 (Li et al., 2012), which is about threefold greater than what we have found in most water boatmen (Fig. 10B). Furthermore, our experiments examined short bouts of swimming from a standstill, where swimming commences with relatively low efficiency. In contrast, measurements of metabolic efficiency generally report average values for sustained swimming (Kaufmann, 1990). Therefore, water boatmen appear capable of achieving a cost of locomotion that is comparable to that of fish of similar size under ideal conditions. However, water boatmen rarely exhibit this ideal because of their intermittent behavior and the inefficiency inherent to their mode of locomotion.

Despite the large influence that the Reynolds number has upon the generation of drag (Fig. 9), it has a complex relationship with swimming energetics. Neither the cost of transport nor the efficiency of swimming exhibits a clear dependency on Reynolds number (Fig. 10). Although these measures of energetic performance depend on *Re*-dependent hydrodynamics (Eqns 15–19), fluid forces also affect the behavior of a swimmer. For instance, the relatively large
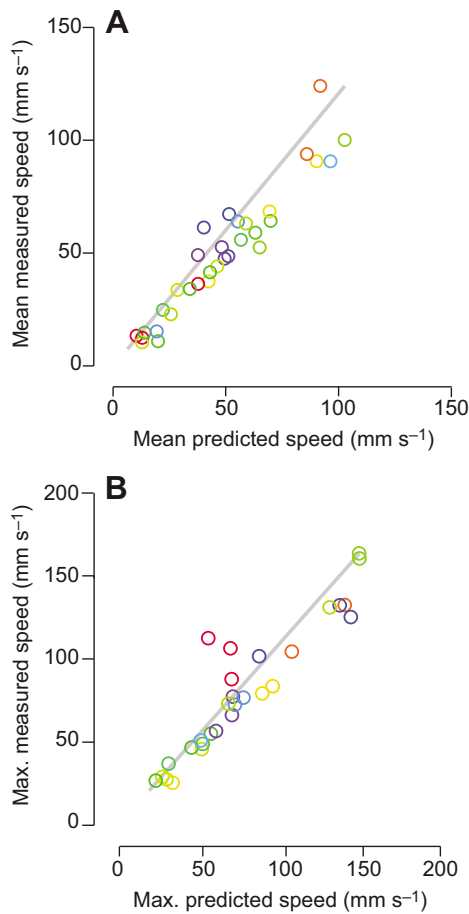
Fig. 7. Testing the accuracy of a forward-dynamic model of free swimming. We tested predictions of both the mean and maximum body speed during a swimming cycle for free-swimming water boatmen. For both measurements, deviation from the unity line (as indicated by the coefficient of determination) indicates inaccuracy of the model. For each water boatman (represented by a different color), multiple power strokes were evaluated (up to three per individual). (A) The model predicted about 90% of the variation in measurements of mean swimming speed (R^2=0.90, N=13). (B) The model similarly approximated the maximum speed of free swimming (R^2=0.85, N=13).
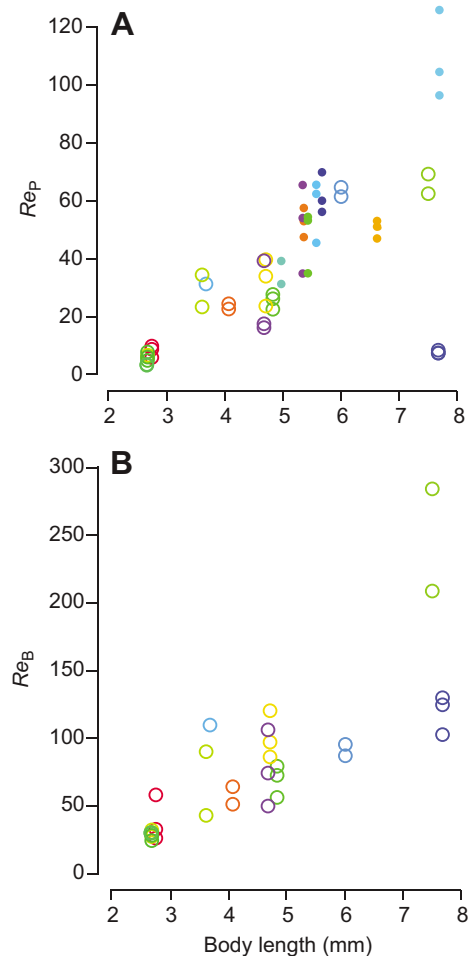

Fig. 8. Measurements of the Reynolds number of the paddle and body of water boatmen. For each water boatman (represented by a different color), multiple power strokes were evaluated (up to three per individual). (A) The Reynolds number of the paddle (Re_P) for tethered (filled circles, N=13) and free-swimming (open circles, N=9) water boatmen of varying body length. (B) The Reynolds number for the body (Re_B) of free-swimming water boatmen (N=13).

drag coefficient encountered by a smaller water boatman may cause the animal to paddle more slowly than a larger animal (supplementary material Fig. S1) and consequently move with greater energetic economy. Therefore, the fluid forces that determine energetics also affect behavioral decisions and the force-generating capacity of muscle, which affect the kinematics that create fluid forces. Given this feedback loop, it is perhaps unsurprising that swimming energetics do not clearly vary with Reynolds number.

Swimming at intermediate Reynolds numbers

Our results illustrate the high sensitivity of propulsion to differences in size and speed at intermediate Reynolds numbers. In this domain, viscous interactions mediate the generation of body drag and propulsion to create force coefficients that may vary by an order of magnitude (Fig. 9) within a relatively narrow range of Reynolds numbers ($10<Re<100$). It is therefore interesting to consider how other strategies for generating propulsion may also vary with size for other animals within this regime. For example, copepods ($100<Re<1000$) propagate a wake from their antennae to abdominal paddles during impulsive 'hopping' (Borazjani et al., 2010). This mechanism could fail as a result of viscous attenuation at lower

Reynolds numbers, or could lack the necessary cohesion at larger scales. Therefore, this mechanism of propulsion is likely to function only within a finite range of Reynolds numbers. Pteropods generate lift and thrust ($1<Re<1000$) with flexible wing-like appendages, which employ a variety of 3D motions (Chang and Yen, 2012). Given the scale dependency of propulsion, a kinematic pattern exhibited by a small pteropod may generate forces that contrast with those of a large pteropod that moves in a similar way. As exhibited by the water boatmen (Fig. 10), the relationship between the hydrodynamics and energetics of swimming is complicated by the influence of fluid forces on behavior. Nonetheless, this fascinating regime illustrates how the performance of locomotion critically hinges on the highly scale-dependent properties of fluid dynamics.

MATERIALS AND METHODS
Animals
Insects were collected between June 2012 and August 2013 from the University of California National Reserve Rancho San Joaquin Marsh (RAMS App. no. 25020, Reservation no. 28126, Irvine, CA, USA). Collected insects were held at 21–24°C in pond water until used in an experiment. Tethered force measurements on nine individuals were
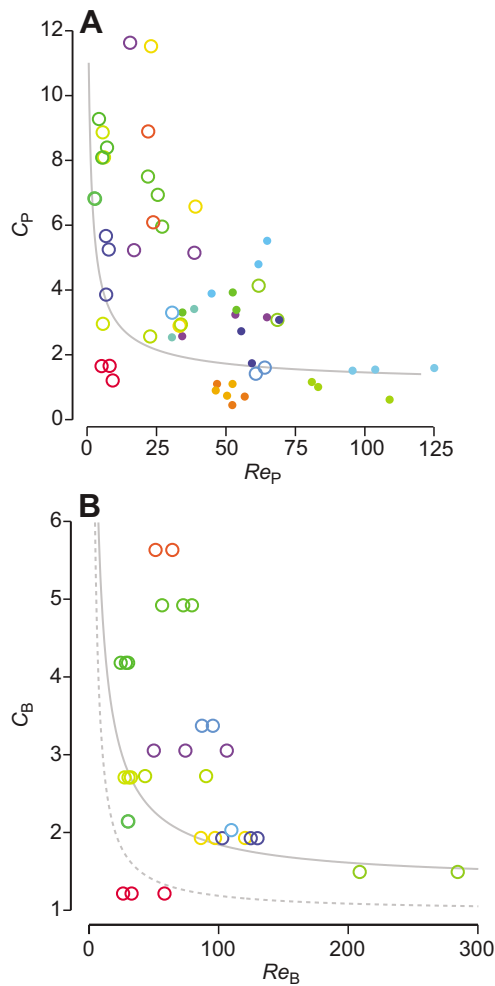
Fig. 9. Drag coefficients for the paddle and body, as a function of the Reynolds number. (A) The drag coefficient of the paddle (C_P) for free swimming (open circles, N=13) and tethered swimming (filled circles, N=9) was calculated by non-linear optimization (Fig. 3A,B). The drag on a cylinder (gray curve) is plotted for comparison. (B) The optimization for free swimming also determined the drag coefficient of the body (C_B) for free swimming. The drag on a sphere due to both pressure drag and skin friction (solid curve) and solely to skin friction (dashed curve) are plotted for comparison.

Fig. 10. The energetics of swimming at intermediate Reynolds numbers. For each water boatman (represented by a different color), multiple power strokes were evaluated (up to three per individual, N=13). (A) The cost of transport (γ) for a swimming boatman (Eqn 15) varies by more than an order of magnitude in a manner that does not correlate with the Reynolds number of a boatman (Re_B). (B) The Reynolds number is similarly not well correlated with the efficiency of swimming (η_K) (Eqn 14).

successfully completed, each within 1 week of collection. The animals used in the tethering experiments ranged in body mass between 4.98 and 8.78 g (6.17±1.23 g, mean ± 1 s.d., N=9). Video recordings of free swimming were completed for 13 individuals, each within 2 weeks of collection. The animals used in the free-swimming experiments ranged in body mass between 2.66 and 7.69 g (4.42±1.72 g, N=13). Prior to all experiments, the wet mass of each water boatman was recorded on a fine scale (Denver Instrument Company, Bohemia, NY, USA) by extracting the animal from the water, gently drying the surface of the body with a Kimwipe (Kimtech Science, Roswell, GA, USA) and then anesthetizing it by perfusion with CO_2.

Thrust measurements
We measured the thrust generated by tethered water boatmen as a basis for testing hydrodynamic models. The tether was composed of twisted Teflon-coated stainless steel wire (0.1143 mm diameter, ~11 mm in length, A-M Systems, Inc., Everett, WA, USA) that was attached to the first dorsal segment of hardened cuticle. This was achieved with a flowable, light-cured dental composite (Prime-Dent, Prime Dental Manufacturing, Chicago, IL, USA), which was also used to anchor the tether to a surface that was positioned with a micro-manipulator. The micro-manipulator translated the animal to the center of a water-filled well (25×50 mm in width), submerged in deionized
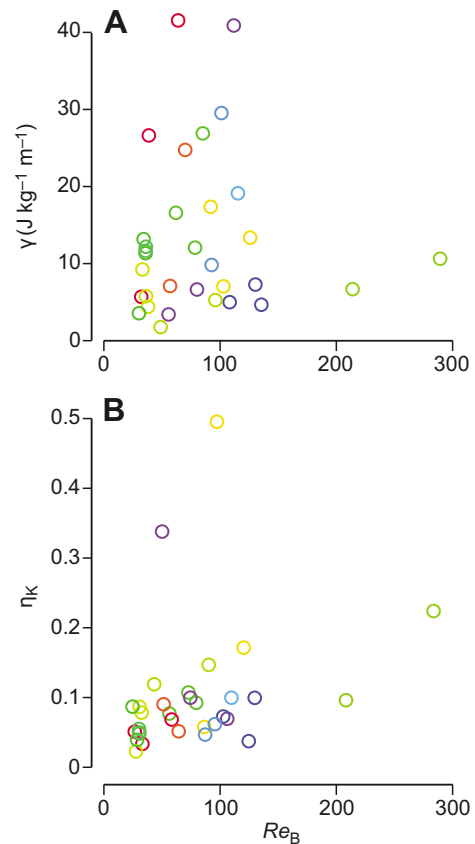
water at a depth of 6 mm at 22°C. The resonant frequency of the tether with an attached water boatman exceeded 300 Hz, which was sufficiently high to exceed the domain of our measurements and thereby not present resonance artifacts. Tether deflections during experiments did not exceed 1% of the length of the tether, which was well within the assumptions of the low-deflection beam theory that we employed in our calibrations (detailed below).

The thrust measurements were based on recordings of tether deflections that were created during swimming. This was achieved with an optical technique that used a laser with integrated sheet-generating optics (5 mW, 670 nm, Lasiris, StockerYale Canada Inc., Quebec, Canada), which was focused onto the mound of glue that affixed the insect to the tether (Fig. 1). The laser sheet was then focused in the vertical direction with a cylindrical lens (6.25 mm diameter, 100 mm focal length, Edmond Industrial Optics, Barrington, NJ, USA). The focused light and shadow cast by the mound were aligned with a photosensor (OSI Optoelectronics, Camarillo, CA, USA), which detected the position of the edge of the shadow. This was achieved with a custom-built amplifier designed for an earlier study (Lehmann and Dickinson, 1997). As the insect generated thrust during an experiment, the voltage changes inducted by the motion of the tether were recorded at 100 kHz by a National Instruments DAQ (NI USB-6009, Trabuco Canyon, CA, USA) and custom-written MATLAB software (v 2012a, MathWorks, Natick, MA, USA). After completing a series of successful recordings, the water boatman was anesthetized and killed through heat exposure by replacing the water within the well with 60°C water until limb movements ceased.

We performed a calibration in two parts to determine thrust from the recordings of the optical sensor. The first part determined the relationship

between the reading of the optical sensor and the tether deflection. This was achieved by recording the sensor voltage as we moved the tethered insect, and hence the shadow cast on the sensor, with a digital actuator (Mitutoyo Corp., Kawasaki, Kanagawa, Japan) in increments of 2–10 μm over the range of recorded voltage. The voltage reported for each tether position was recorded as the mean value of a 1 s recording at 100 kHz. We characterized how voltage varied with the position of the tether by a non-linear least-squares fit of a smoothing spline (the 'spaps' function in MATLAB, Fig. 2A) to our recorded values. This spline provided the means to transform sensor voltage recordings into values of tether deflection.

The second part of the calibration determined the force required to deflect the tether. We removed the well containing water and rotated the entire apparatus (i.e. laser, tethered insect, micro-manipulator, lens and photosensor) by 90 deg, such that gravity was aligned along the plane of tether deflection. We measured the deflection of the tether under load for at least 15 small weights in ~10 mg increments. Each weight was hung near the distal end of the tether, at its intersection with the glue that attached the water boatman. After applying each weight, the digital actuator at the proximal end of the tether was adjusted to raise the tether tip to its undeflected position. The position of the tip was monitored during this adjustment by the voltage reading of the optical sensor. The deflection generated by the weight was recorded as the actuator displacement that was necessary to return the tether to its unloaded position. The relationship between weight and deflection was used to determine the flexural stiffness of the tether (EI). This was achieved with the following relationship for a point-load (F) applied at the distal end of a cantilever beam at low deflection (Gere, 2001):

$$EI = \frac{l_L^3}{3}\left(\frac{F}{\delta}\right), \tag{1}$$

where δ is the tether deflection and l_L is the distance between the base of the tether and the point of load application. The ratio F/δ was calculated as the slope of the force verses deflection relationship for all deflection measurements using linear least-squares with a zero intercept (Fig. 2B). This measure of flexural stiffness was used to calculate the thrust generated during an experiment by applying the same principle for a cantilever beam in the following relationship:

$$T_M = \delta\frac{3EI}{l_T^3}, \tag{2}$$

where T_M is measured thrust and l_T is the distance between the center of the insect's body and the base of the tether.

Tethered swimming kinematics

The tethering experiments were recorded with high-speed video to measure the kinematics of paddling, which provided variables for our mathematical models of thrust. During the experiments, tethered insects were backlit with an array of white LED lights and viewed from the ventral perspective using a front-surface mirror (Edmond Industrial Optics, Barrington, NJ, USA) positioned beneath the chamber and oriented at 45 deg. This mirror allowed for a camera directed toward the side of the well to view the water boatman from below. Recordings were executed at 3000 frames s^{-1} with a resolution of 512×512 pixels using a 1024 Photron camera (Photron Inc., San Diego, CA, USA) that was fitted with a macro lens (Micro-NIKKOR P.C Auto 55 mm with two Nikon PK-13 27.5 mm extension tubes, Nikon US, La Jolla, CA, USA) to record a ~16 mm square field of view. Three swimming cycles (i.e. power and recovery strokes) were recorded and analyzed for each individual.

We manually tracked landmarks on the body and a single hindleg to acquire paddling kinematics from video recordings using custom-written MATLAB software. The body was described by two coordinates for its anterior and posterior margins along the mid-sagittal plane (points 1 and 2, Fig. 2C). The paddle was tracked by coordinates for the proximal and distal ends (points 3 and 4 respectively, Fig. 2C) of the tarsus (i.e. paddle), the most distal segment of the metathoracic hindleg. We defined the wrist angle (ϕ) as the angular position of point 3 with respect to the body midpoint. Changes in the direction of the wrist angle were used to identify the

initiation and completion of power strokes. The speed and orientation of the paddle were variables in our modeling (described below). Orientation was measured with the paddle angle (θ), which was defined with respect to the body midline (Fig. 2C) and factored into the calculation of thrust (described below, Fig. 2D,E). The paddle speed was calculated discretely as the product of the frame rate and the displacement of the paddle midpoint (i.e. spatial mean of points 3 and 4). These values were filtered with a least-squared fit of a smoothing spline (the 'spaps' function in MATLAB).

Morphometrics for each water boatman were measured after tethering experiments. Images were captured with a high-resolution camera (Zeiss AxioCam HRc) mounted onto a dissecting microscope (Zeiss SteREO Discovery V20, Thornwood, NY, USA). Linear dimensions and area measurements were performed with software (AxioVision Release 4.8.2, Zeiss) that autoscaled images according to the magnification of the microscope. The two lengths (l_T and l_L) used in our tethering calibration were measured from a photograph of the insect while still attached to the tether. The body of each individual was additionally photographed from dorsal, lateral and ventral perspectives. The maximum width (l_w) and depth (l_d) of the body were used to calculate its projected area (s_B), assuming an elliptical shape (i.e. $s_B=1/4\,\pi\,l_w l_d$) and body length (l_B) provided a general metric of size. Using a photograph at higher magnification, the hindlimb was measured for the length of each segment: the femur, tibia and tarsus. We measured the area encompassed by the setae of the paddle (s_P) by excising the tarsus and splaying it on a drop of water under a coverslip (Fig. 2F). The area was measured by tracing the peripheral shape of all setae in a digital photograph of the splayed tarsus.

Mathematical models of thrust

We tested mathematical models of the thrust generated by a tethered water boatman. One interest was in determining whether thrust during a power stroke was generated primarily by pressure drag or skin friction. The equations for these models treated the speed (u_P) and angle (θ) of the paddle as quantities that varied with time, as described by our measured kinematics (Fig. 2C–E). The remaining quantities were assumed to be fixed parameters, although our optimization algorithm (detailed below) permitted the force coefficients to vary among power strokes for an individual. Thrust created by pressure drag (T_D) upon the two paddles was modeled with the following equation (Lamb, 1945):

$$T_D = -\rho C_P s_P u_P^2 \sin\theta, \tag{3}$$

where C_P is the drag coefficient for a paddle. Thrust generated by skin friction on the two paddles (T_V) was modeled with the following equation (Lamb, 1945):

$$T_v = -2\mu C_V \frac{s_P}{l_P} u_P \sin\theta, \tag{4}$$

where C_V is the skin friction coefficient. We used these equations to formulate instantaneous predictions of thrust, based on morphometrics for each individual and the kinematics measured for each power stroke during tethered swimming. This quasi-steady approach neglected an explicit consideration of forces generated by interactions between the wake and the body and paddles of the water boatmen. However, if such forces were important, then they would have affected the values for force coefficients that we found by our optimization algorithm. This model also assumes negligible force generation by the recovery stroke. This was supported by our initial tethered recordings, which indicated that no observable forces were exerted against the tether during the recovery stroke.

For both models, we used an optimization algorithm to determine the values for the force coefficients that best matched the thrust measurements (Fig. 3A). This worked by separately calculating the thrust generated by pressure drag (Eqn 3) and skin friction (Eqn 4) iteratively with varying values for the force coefficient (either C_P or C_V). Using the least-squares method, the optimization selected the value for each coefficient that minimized the error between predicted and measured thrust, defined as the sum of squared differences over the duration of the power stroke (implemented with the 'lsqcurvefit' function in the optimization toolbox in MATLAB, v R2013a). Therefore, our test of each form of drag used the ideal force coefficient that could be found for each drag equation.

As described in the Introduction, thrust may additionally be generated by the acceleration reaction on the paddle. We modeled the acceleration reaction (T_A) with the following equation (Lamb, 1945):

$$T_A = -2\alpha_P \rho v_P u'_P \, , \tag{5}$$

where α_P is the added mass coefficient and v_P is the volume of water around the paddle, modeled as a cylinder with a length and diameter equal to the average chord width of the tarsus (i.e. $v_P = \pi s_P^2/4l_P$). Paddle acceleration (u'_P) was calculated as the first derivative of the smoothing spline that was fitted to our discrete measurements of paddle velocity. The acceleration reaction is a force that is thought to act in addition to drag to generate thrust, but is greatest at the start and end of a power stroke, when drag is at its lowest level (Daniel, 1984). Therefore, we subtracted our predictions of drag (Eqns 3 and 4) from our measurements to isolate the component of our measurements due to acceleration reaction. We fitted predictions of acceleration reaction (Eqn 6) to this residual force by finding the added mass coefficient that minimized differences between the residual force and predicted acceleration reaction. This was executed by the same non-linear least-squares optimization used to fit the drag coefficients to measured thrust (Fig. 3A).

We compared the accuracy of different models of thrust by testing their ability to predict the momentum generated during a power stroke. Momentum was determined by integrating thrust over the duration of a power stroke using the trapezoidal rule (implemented by the 'trapz' function in MATLAB). Predictions of momentum were tested for three models of thrust. The first treated thrust as being generated entirely by pressure drag on the paddle. For the second model, thrust was calculated as the sum of pressure drag and the acceleration reaction. The third model considered drag to be entirely generated by skin friction on the paddle. We calculated the coefficient of determination for the predictions of each model against our momentum measurements to describe the proportion of variation in the measurements that were predicted by each model and thereby provide a basis for comparing their accuracy.

Free-swimming hydrodynamics

We considered the hydrodynamics of free swimming by first measuring kinematics. Individual insects were placed into a 50 mm diameter Petri dish and filmed at 500 frames s^{-1} from the dorsal perspective (Photron Inc. FASTCAM 1024, San Diego, CA, USA), using a Nikon Micro-NIKKOR 55 mm lens (Nikon USA) with a field of view of 4.3×4.3 cm at 1024×1024 pixels. After the videos were recorded, each insect was killed for measurements of body mass and morphometrics (as for the tethering experiments). We recorded the position of the body and one of the hindlegs from the video recording using the methods for tethered kinematics described above. Only sequences of straight swimming over at least three power strokes were considered and only three were analyzed for each water boatman. We calculated the Reynolds number of the paddle (Re_P) to identify its hydrodynamic regime with the following equation (Lamb, 1945):

$$Re_P = \frac{\rho \overline{u} s_P}{\mu l_P} \, , \tag{6}$$

where ρ and μ are, respectively, the density and dynamic viscosity of water, $\overline{u}$ is the mean speed over the power stroke, and s_P and l_P are, respectively, the projected area and chord length of the paddle. The Reynolds number for the body (Re_B) was similarly calculated as follows:

$$Re_B = \frac{\rho \overline{u_B} l_w}{\mu} \, , \tag{7}$$

where $\overline{u_B}$ is the average body speed over the entire swimming sequence.

We modeled free swimming with a forward dynamic model that considered the hydrodynamics of paddling and the body. As described in Results, we learned from our force measurements that the pressure drag model (Eqn 3) offered a good approximation for the thrust generated by a tethered water boatman. We therefore assumed this model of thrust in our forward dynamic simulations, which determined the total force on the body as the sum of this thrust and drag on the body. Because both of these forces depend on the velocity of the body, these dynamics may be formulated by the following first-order differential equation:

$$(m + \alpha_B \rho v_B) u'_B = \rho C_P s_P (u_P - \sin\theta u_B)^2 \sin\theta - \frac{1}{2}\rho C_B s_B u_B^2 \, , \tag{8}$$

where u_B is the body's forward velocity and C_B is the drag coefficient of the body. Our simulations solved this equation numerically using an explicit fourth-order Runge–Kutta method (the 'ode45' function in MATLAB) with an initial speed set equal to our measurement at the beginning of the power stroke. Positive values predicted by the model correspond to forward motion, which is why the drag on the body (i.e. the final term in Eqn 8) has a negative sign. Therefore, each simulation solved for changes in the forward motion of the body from the thrust calculated from measurements of paddle speed and angle. As for the modeling of thrust, our forward dynamic model neglected an explicit consideration of forces generated by interactions between the wake and the body and paddles of the water boatmen, but instead included the force coefficients. The model did not explicitly consider forces generated by the recovery stroke, which was supported by the lack of force observed in these periods from our tethering experiments. Nonetheless, our approach allows for the possibility that the paddles can contribute to the drag coefficient that we measured for the body.

We solved for the force coefficients using an optimization algorithm that was based on our forward dynamic model (Fig. 3B). We allowed the drag coefficient on the paddle to vary among the power strokes within a swimming sequence, because of the possible differences in stroke kinematics. However, the optimization did assume a constant value for the drag coefficient of the body because its geometry did not appreciably vary during a sequence. Similar to the analysis of our tethering experiments, the non-linear optimization used a least-squares approach to solve for the drag coefficient values for the body and paddle that minimized deviation between predicted and measured body speed over a series of simulations (e.g. Fig. 3C).

We examined variation in the drag coefficients with respect to the Reynolds number to determine whether skin friction is a contributor to propulsion. For comparison, we considered the same relationship for a sphere and a circular cylinder. For flow normal to a cylinder, the drag coefficient has empirically been shown to vary with Re in a manner approximated by the following equation (White, 1991):

$$C_P = 1 + 10Re^{-2/3} \, , \tag{9}$$

where Re is defined with the diameter of the cylinder as the characteristic length. We compared the drag on the body with that of a sphere. Empirical measurements for the drag on a sphere vary according to the following equation (Mikhailov and Freire, 2013):

$$C_B = \frac{3808(797.01 + 168.26Re + 1.1245Re^2)}{681Re(183.72 + 13.862Re - Re^2/71154)} \, . \tag{10}$$

Stokes law approximates the component of this drag due solely to skin friction (Lamb, 1945):

$$C_B = \frac{24}{Re} \, . \tag{11}$$

Swimming energetics

We used the results of our forward dynamic modeling to examine the energetics of free swimming. These calculations were based on instantaneous calculations of the power generated by the paddle (P_P), the thrust power (P_T) and the power lost to drag (P_D):

$$P_P = -\rho C_P s_P (u_P - \sin\theta u_B)^3 \, , \tag{12}$$

$$P_T = \rho C_P s_P (u_P - \sin\theta u_B)^2 \sin\theta u_B \, , \tag{13}$$

$$P_D = -\frac{1}{2}\rho C_B s_B u_B^3 \, . \tag{14}$$

The power generated by the paddle was applied to power for thrust and the generation of lateral forces. Each of the three forms of power listed above were integrated over time (using the 'trapz' function in MATLAB) to calculate the energies generated by the paddle and applied to thrust (respectively, E_P and E_T) and the energy lost to drag (E_D). The kinetic energy of the body was therefore equal to the difference between the energy of thrust and drag:

$$E_K = E_T - E_D \, . \tag{15}$$

As a means of testing the internal consistency of our calculations, we verified that the instantaneous values yielded by Eqn 15 were equivalent to the following direct calculation for the kinetic energy:

$$E_K = \frac{1}{2} m u_B^2 . \qquad (16)$$

These calculations of energy were used to determine the efficiency and energetic cost of swimming. By our accounting, inefficiency was created by the loss of energy generated by the paddle to the generation of lateral force and drag. Energy lost to lateral force was reflected by a reduction of thrust efficiency (η_T), which was calculated by the following ratio:

$$\eta_T = \frac{\Delta E_T}{\Delta E_P} , \qquad (17)$$

where Δ denotes a change in energy from the start to the end of a propulsive cycle (power and recovery strokes). Energetic loses by both lateral force and drag created a reduction in the propulsive efficiency, which therefore provided a comprehensive metric of mechanical efficiency. The propulsive efficiency was calculated as the time-averaged kinetic energy over a swimming cycle, divided by the energy generated by the paddle over the power stroke:

$$\eta_K = \frac{\overline{E}_K}{\Delta E_P} . \qquad (18)$$

A related metric of energetic performance is the cost of transport (γ), which provides a measure of energetic fuel economy. We calculated the cost of transport as follows:

$$\gamma = \frac{\Delta E_P}{\Delta x m_B} , \qquad (19)$$

where Δx is the body displacement over a swimming cycle. We examined how these energetic quantities varied with the Reynolds number of water boatmen.

References
Alexander, R. M. N. (1968). *Animal Mechanics*. Seattle, WA: University of Washington Press.
Alexander, R. M. N. (2003). *Principles of Animal Locomotion*. Princeton, NJ: Princeton University Press.
Blake, R. W. (1986). Hydrodynamics of swimming in the water boatman, *Cenocorixa bifida*. *Can. J. Zool.* **64**, 1606-1613.
Borazjani, I., Sotiropoulos, F., Malkiel, E. and Katz, J. (2010). On the role of copepod antennae in the production of hydrodynamic force during hopping. *J. Exp. Biol.* **213**, 3019-3035.
Chang, Y. and Yen, J. (2012). Swimming in the intermediate Reynolds range: kinematics of the pteropod *Limacina helicina*. *Integr. Comp. Biol.* **52**, 597-615.
Cheer, A. Y. L. and Koehl, M. A. R. (1987a). Fluid flow through filtering appendages of insects. *Math. Med. Biol.* **4**, 185-199.
Cheer, A. Y. L. and Koehl, M. A. R. (1987b). Paddles and rakes: fluid flow through bristled appendages of small organisms. *J. Theor. Biol.* **129**, 17-39.
Curtin, N. A. and Woledge, R. C. (1993). Efficiency of energy conservation during sinusoidal movement of red muscle fibers from the dogfish *Scyliorhinus canicula*. *J. Exp. Biol.* **185**, 195-206.
Daniel, T. L. (1984). Unsteady aspects of aquatic locomotion. *Am. Zool.* **24**, 121-134.
Dickinson, M. H. (1996). Unsteady mechanisms of force generation in aquatic and aerial locomotion. *Am. Zool.* **36**, 537-554.
Dickinson, M. H., Lehmann, F.-O. and Sane, S. P. (1999). Wing rotation and the aerodynamic basis of insect flight. *Science* **284**, 1954-1960.
Frith, H. R. and Blake, R. W. (1991). Mechanics of the startle response in the northern pike (*Esox lucius*). *Can. J. Zool.* **69**, 2831-2839.
Gere, J. M. (2001). *Mechanics of Materials*. Cheltenham, UK: Nelson Thornes Ltd.
Hoerner, S. F. (1965). *Fluid-Dynamic Drag*. Brick Town, NJ: Hoerner Fluid Dynamics.
Jiang, H. and Kiørboe, T. (2011). Propulsion efficiency and imposed flow fields of a copepod jump. *J. Exp. Biol.* **214**, 476-486.
Jordan, C. E. (1992). A model of rapid-start swimming at intermediate Reynolds number: undulatory locomotion in the chaetognath *Sagitta elegans*. *J. Exp. Biol.* **163**, 119-137.
Kaufmann, R. (1990). Respiratory cost of swimming in larval and juvenile cyprinids. *J. Exp. Biol.* **150**, 343-366.
Lamb, H. (1945). *Hydrodynamics*. New York, NY: Dover.
Lehmann, F.-O. and Dickinson, M. H. (1997). The changes in power requirements and muscle efficiency during elevated force production in the fruit fly *Drosophila melanogaster*. *J. Exp. Biol.* **200**, 1133-1143.
Li, G., Müller, U. K., van Leeuwen, J. L. and Liu, H. (2012). Body dynamics and hydrodynamics of swimming fish larvae: a computational study. *J. Exp. Biol.* **215**, 4015-4033.
Lighthill, J. (1971). Large-amplitude elongated-body theory of fish locomotion. *Proc. R. Soc. B* **179**, 125-138.
McHenry, M. J., Azizi, E. and Strother, J. A. (2003). The hydrodynamics of locomotion at intermediate Reynolds numbers: undulatory swimming in ascidian larvae (*Botrylloides* sp.). *J. Exp. Biol.* **206**, 327-343.
Mikhailov, M. D. and Freire, A. P. (2012). The drag coefficient of a sphere: an approximation using Shanks transform. *Powder Technol.* **237**, 432-435.
Miller, L. A. and Peskin, C. S. (2009). Flexible clap and fling in tiny insect flight. *J. Exp. Biol.* **212**, 3076-3090.
Nachtigall, W. (1960). Über kinematik, dynamik und energetik des schwilimens einheimischer dytisciden. *Z. Vgl. Physiol.* **43**, 48-118.
Nachtigall, W. and Bilo, D. (1965). Die strömungsmechanik des dytiscus-rumpfes. *Z. Vgl. Physiol.* **50**, 371-401.
Tytell, E. D. (2004). The hydrodynamics of eel swimming II. Effect of swimming speed. *J. Exp. Biol.* **207**, 3265-3279.
Tytell, E. D. and Lauder, G. V. (2008). Hydrodynamics of the escape response in bluegill sunfish, *Lepomis macrochirus*. *J. Exp. Biol.* **211**, 3359-3369.
Videler, J. J. (1993). *Fish Swimming*. New York, NY: Springer.
Weihs, D. (1972). A hydrodynamical analysis of fish turning manoeuvres. *Proc. R. Soc. Lond. B* **182**, 59-72.
White, F. (1991). *Viscous Fluid Flow*. New York, NY: McGraw Hill.
Williams, T. A. (1994). Locomotion in developing *Artemia* larvae: mechanical analysis of antennal propulsors based on large-scale physical models. *Biol. Bull.* **187**, 156-163.
Wu, T. Y. (1971). Hydromechanics of swimming propulsion. Part 2. Some optimum shape problems. *J. Fluid Mech.* **46**, 521-544.
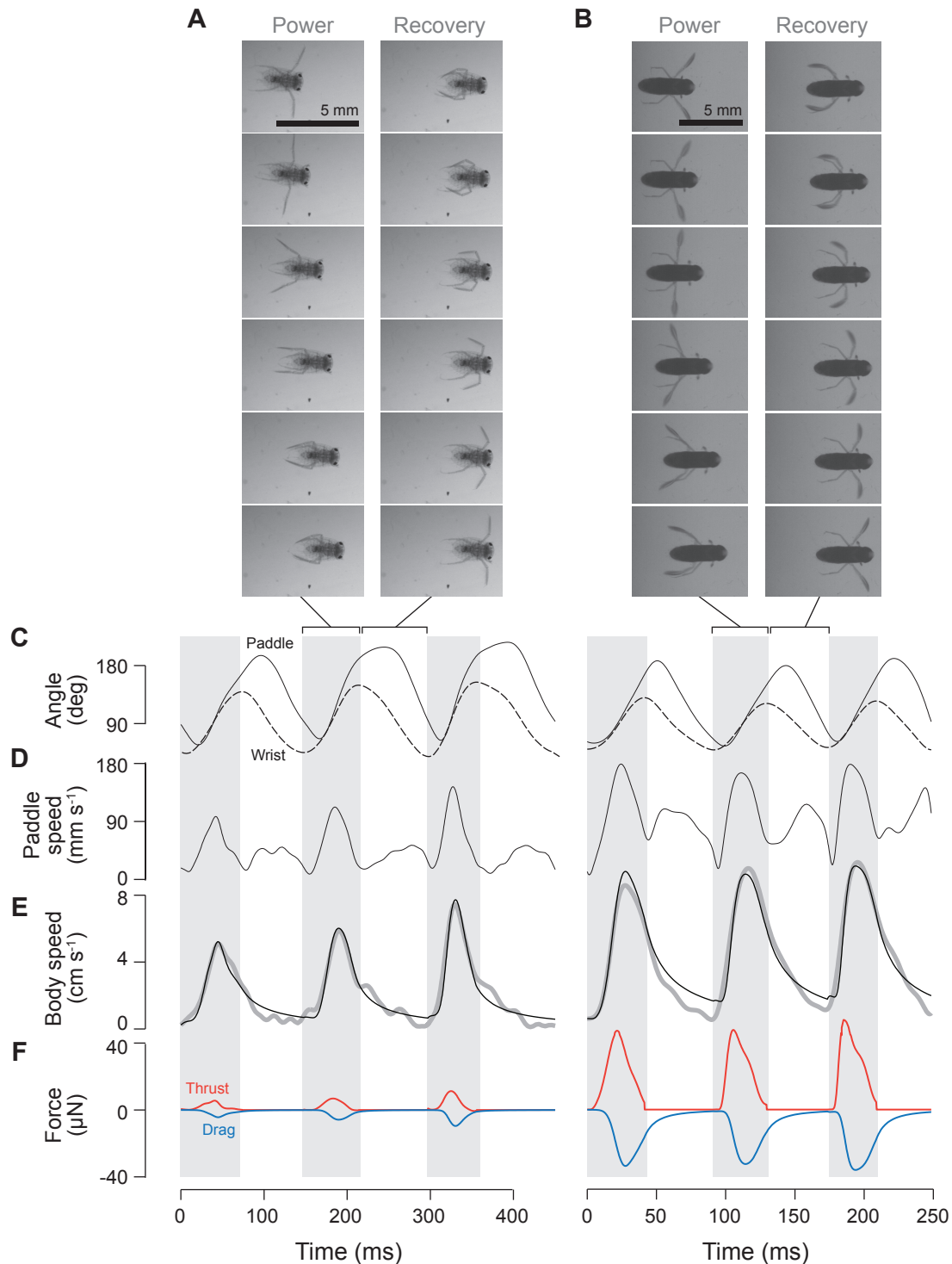
Fig. S1 Swimming kinematics of two boatmen compared. Frames of high-speed video recordings of (A) a small boatman (Re = 39) at 14 ms intervals and (B) a larger boatman (Re = 80) at 8 ms intervals. Kinematics measurements and calculations of thrust and drag are shown as in Fig. 6. (C) Reversals in the wrist angle were used to define the duration of the power strokes (gray bars). We measured the (C) angle and (D) speed of the paddle (relative to the body) to model thrust. Forward dynamic simulations included thrust and drag on the body to predict changes in the speed of the body over time (Eqn. 8). (E) These predictions of speed (black curve) were tested against measurements (gray curve) for the same sequence. (F) The thrust (red curve) predicted by this model peaked at around the middle of the body stroke as the total drag generated by the body and appendages (blue curve) lagged behind in time, as the body gained speed due to the thrust impulse.